First Principles Material Screening and Discovery of Perovskite Electrolytes for Proton-**Conducting Solid Oxide Fuel Cells** Nicholas A. Szaro^a, Salai Cheettu Ammal^a, Fanglin Chen^b, Andreas Heyden^a* ^a Department of Chemical Engineering, University of South Carolina, 301 South Main Street, Columbia, South Carolina 29208, United States ^b Department of Mechanical Engineering, University of South Carolina, 300 South Main Street, Columbia, South Carolina 29208, United States *Email: <u>heyden@cec.sc.edu</u>

Abstract

15

16

17

18

19

20

21

22

23

24

25

26

27

28

29

30

31

32

33

The perovskite oxide family is renowned for its ability to be modulated with elemental doping to tune desirable macroscopic properties. Perovskite oxides are commonly used as proton-conducting ceramic (PCC) electrolytes for solid-oxide fuel cells. PCC electrolytes must have thermodynamic stability in both oxidizing and reducing environments, low electronic conductivity, and the ability to readily form protonic defects. To help discover new PCC electrolyte materials and to understand the role of different elements and compositions on material properties, high-throughput materials screening together with first principles materials science can be utilized to scan a large elemental phase space. In this study, we conduct a highthroughput scan of 4793 materials to determine how different cation species modulate thermodynamic stability, electronic conductivity, and defect formation. Our filtering analysis identifies 116 materials (including BaZrO₃ and BaCeO₃) that are electronically inactive and thermodynamically stable under reducing and oxidizing conditions. Furthermore, we identity 43 materials (including BaZrO₃) that are also thermodynamically stable under a pure CO₂ environment. For all the 116 materials, we conducted a thermodynamic analysis of oxygen vacancy and protonic defect formation to identify trends in ionic conductivity. This study provides a supplemental understanding of the role of elemental identity and doping ratios on material stability and activity that can aid the design of new perovskite oxides for protonconducting applications.

34

35

Keywords: Solid oxide fuel cells; Proton-conducting ceramic; Material Discovery; Perovskite

1. Introduction

36

37

38

39

40

41

42

43

44

45

46

47

48

49

50

51

52

53

54

55

56

57

58

Solid oxide fuel cells (SOFCs) are electrochemical devices that directly oxidize hydrogen and hydrocarbon-based fuels with a higher theoretical efficiency relative to the thermochemical combustion of hydrogen and hydrocarbon-based fuels [1]. For oxide-conducting SOFCs (O-SOFCs), the anode oxidizes incoming fuel and consumes negative oxide ions (O²⁻), the cathode reduces incoming oxygen and produces O²-, and the electrolyte layer conducts O²- ions from one electrode to the other without the conduction of electrons. To overcome high activation energies associated with electrode kinetics and ionic conduction, high operating temperatures (e.g., > 800 °C) are required which limits the practical applications and commercialization of SOFCs [2,3]. The electrolyte plays a vital role in determining the operating temperature of SOFCs based on the electrolyte's ability to conduct ions between the electrodes. Common O-SOFC electrolytes include YSZ, LSGM, and GDC [4-6] and require a typical functioning temperature of 700-1000 °C to exhibit high ionic conductivity. Therefore, O-SOFCs suffer from high operational costs and premature aging due to mechanical stresses [4,7]. A possible solution to lower the electrolyte operating temperature is the utilization of proton-conducting solid oxide fuel cells (P-SOFCs) [8,9]. Proton-conducting ceramics (PCCs) have displayed promising ionic conductivity at temperatures as low as 400 °C [10]. Therefore, PCCs have attracted significant interest in the development of intermediate temperature (e.g., ~ 650 – 800 °C) SOFCs. The perovskite oxide material family with general formula of ABO₃ (Figure 1(a)), where the A-site being an alkali metal, an alkaline earth, or a rare earth metal, and the B-site being a transition metal, has received significant research interest for proton-conducting applications [11]. The current state-of-the-art P-SOFC electrolytes are the acceptor-doped PCCs based on BaZrO₃ (BZO, Figure 1(b)) and BaCeO₃ (BCO, Figure 1(c)). BZO suffers from ionic conductivity

problems due to high grain boundary resistance, and BCO suffers from material instability in the 59 presence of H₂O and CO₂ [^{12–14}]. To better improve the performance of BZO and BCO, 60 researchers have used elemental doping at the B-site to modulate the ionic conductivity and 61 thermodynamic stability. Zuo et. al. co-doped BCO with Zr and Y to produce the material 62 Ba(Zr_{0.1}Ce_{0.7}Y_{0.2})O_{3- δ} (BZCY7) which was found to display good conductivity ($\sim 9 \times 10^{-1}$ S 63 cm⁻¹ at 700 °C) and thermodynamic stability under CO₂ environments [15,16]. Despite these 64 promising properties, commercial adoption of BZCY7 (and other BZCY conformers) suffers 65 from high manufacturing costs due to high sintering temperatures (> 1550 °C) and from a limited 66 concentration of incorporated protons due to the acceptor-dopant proton trapping effect [17–20]. 67 Beyond the BZO and BCO families, Zhou et. al. reported that the perovskite SmNiO₃ could be a 68 promising PCC for low temperature SOFCs [21]. Brownmillerite, niobate, tantalite, and 69 Ruddlesden-Popper material classes have also received attention as potential PCC materials for 70 intermediate temperature P-SOFC applications [22–24]. However, only a limited number of these 71 72 materials can satisfy most properties required for optimal PCCs at lower temperatures, such as high proton conductivity, low activation energy, chemical stability with neighboring electrode 73 74 layers, and thermodynamic stability under H₂O and CO₂ environments. Understanding the role of 75 cations and the structures of these complex oxides, such as perovskite-based materials, is critical to guide the development of novel PCC materials with high efficiency. 76

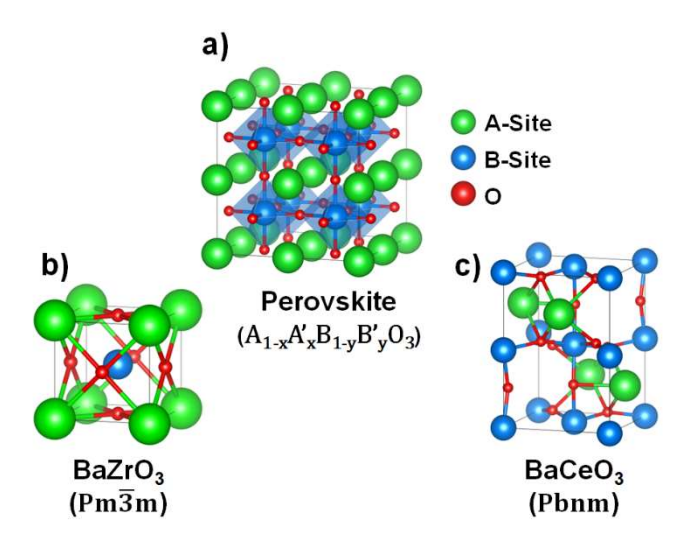


Figure 1: a) General structure of the perovskite oxide (ABO₃) used for all computed compositions in this study, b) cubic unit cell of BaZrO₃, and c) orthorhombic unit cell of BaCeO₃.

78

79

80

81

82

83

84

85

86

87

88

89

90

91

A high-throughput first-principles material discovery and design strategy has been effectively used to identify new materials for O-SOFC applications [25,26], thermionic emission devices [27], solar cell applications [28], and PCCs. For PCCs, Islam et al. [29] sampled over 5000 ternary oxide materials with six formula classes, A_xBO₆, A_xBO₄, A_xB₂O₇, A_xBO₃, A_xB₂O₅, and A_xBO₂, without considering any doping at the A- or B-sites. Thermodynamic stability of these materials in the presence of H₂O at 0 K, proton migration barriers, and proton incorporation capabilities were tested in this study and found that the materials with connected BO₆ octahedra, such as, perovskites YbFeO₃, AcFeO₃, YbCoO₃, and CaFeO₃ ($Pm\bar{3}m$); Tb₂Mo₂O₇ ($Fd\bar{3}m$); Eu₃MoO₇ (P2₁2₁2₁); brownmillerite Sr₂Co₂O₅ (Pnma); Mn₂TeO₆ (P4₂/mnm); and NbMoO₄ and CrMoO₄ (Cmmm), are in general good proton conductors. In terms of water stability, oxides containing A-site cations with high oxidation states and B-site cations including Zr, V, and Mo exhibit good stability, whereas oxides with Co, Ti, and Ce cations tend to degrade in the presence of H₂O. Furthermore, fast proton diffusion is favored along the BO₆ octahedra compared to other types of BO_x polyhedral. Furthermore, no perovskite material yielded a migration barrier greater than 0.97 eV and f-block-containing perovskites displayed a proton

migration barrier range between 0.13 to 0.59 eV. While this study provided a general understanding and guidelines for identifying novel PCC materials from a large set of non-doped ternary oxide materials, introduction of A- and B-site dopants to these materials needs to be explored to further improve the stability and ionic conductivity.

Here, we conducted a density functional theory (DFT) high-throughput screening study of a wide array of perovskite oxides to understand the influence of A- and B-site cations and dopants on proton conductivity and to discover novel PCC materials with good conductivity and phase stability under H₂, H₂O and CO₂ environments. Starting from the database of materials analyzed by Jacobs et. al. [25] and Ma et. al. [27], the materials set is further expanded to 4793 distinct perovskites with a general A_{1-x}A'_xB_{1-y}B'_yO₃ stoichiometry and include binary, tertiary, quaternary, and quinary A- and B-site compositions. Our initial screening based on electronic conductivity (bandgap energy > 2.0 eV) and phase stability under cathode/anode environments resulted in 116 materials. For these compounds, we computed oxygen vacancy formation and hydration energies to determine the thermodynamic baseline of proton conductivity. Additional screening based on thermodynamic stability under CO₂ environment resulted in 43 materials that could satisfy key environmental stability requirements for proton conductors. This computational search serves to help enhance the understanding of the materials chemistry that governs proton conduction, electronic conductivity, and thermodynamic stability for a wide spectrum of perovskite oxides.

2. Methods

92

93

94

95

96

97

98

99

100

101

102

103

104

105

106

107

108

109

110

111

112

113

114

Electronic structure and total energy calculations of the perovskite materials were performed using spin polarized DFT as implemented in the Vienna Ab Initio Simulation Package (VASP) version 5.4.4 [30]. The generalized gradient approximation (GGA) with the Perdew,

Burke, and Ernzerhof (PBE) functional [31,32] was used to evaluate electron exchange-correlation effects. The nuclei and core electrons were represented by the frozen-core projector-augmented wave (PAW) approach [33,34]. All pseudopotentials used in the present study are equivalent to those used by Pymatgen (Python Materials Genomics) v2022.10.22 [35] and the Materials Project [³⁶] to maintain computational setup uniformity for phase stability analysis. For materials containing specific transition metals (e.g., V, Cr, Mn, Fe, Co, Ni), Dudarev's approach for DFT+U calculations is used to correct the inadequate description of localized 3d electrons [37,38]. Effective U-J parameters used for these transition metals are taken from the Materials Project database and these values are tabulated in Table S1 of the Supporting Information. Integration over the Brillouin zone used the Gaussian smearing method ($\sigma = 0.05 \text{ eV}$) for all calculations. The electronic energy and ionic relaxations were converged to 10⁻⁶ eV and 0.02 eV/Å, respectively. All $2 \times 2 \times 2$ supercell calculations (40 atoms per cell) utilized a $4 \times 4 \times 4$ Monkhorst-Pack (MP) k-point mesh consistent with earlier studies [39,25,27]. The planewave cutoff energy of 520 eV was used for all the calculations to be consistent with the computational setup used in the Materials Project database.

115

116

117

118

119

120

121

122

123

124

125

126

127

128

129

130

131

132

133

134

135

136

137

All the perovskite materials chosen here for electronic and thermodynamic stability screenings have a chemical formula of ABO₃ and they do not possess any oxide or proton defects. It is noted that many of these materials may exhibit a degree of oxygen off-stoichiometry or hydrogen defect formation under SOFC operating conditions [²⁵]. Therefore, the ABO₃ materials used in this study represent a set of idealized compounds that can be used to efficiently screen materials and the off-stoichiometry analysis is considered out-of-scope for our first-pass screening study. The tertiary, quaternary, and quinary perovskites were modeled by introducing A- and/or B-site dopants in 12.5% increments with the dopant ratio ranging from 12.5% to 50%,

excluding 37.5% in accordance with the earlier studies by Jacobs et. al. [²⁵] and Ma et. al. [²⁷]. Also, in accordance with the aforementioned studies, a single ordering for doped compounds was considered by introducing dopant atoms as far away from each other as possible on the perovskite sublattice such that the number of permutations is tractable. Ma et al. have shown that different cation orderings, as displayed in Figures S1-5, have little or no effect on the general electronic properties and convex hull stability [²⁷]. Further details regarding the computed configurations are outlined in section S1 of the Supporting Information.

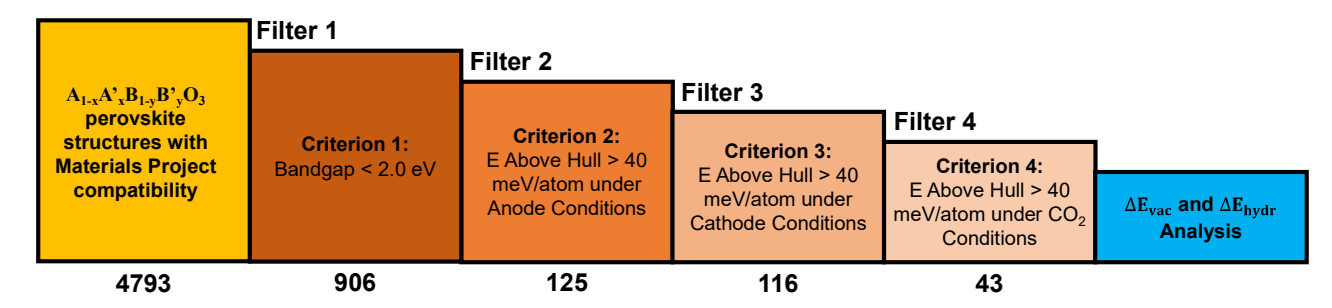


Figure 2: Computational workflow for the DFT-based high-throughput screening process used in this study. The number below each filter box refers to the number of materials that pass the corresponding filter criterion.

The filtering methodology used for the high-throughput screening of PCC materials is presented in Figure 2. Our initial data set has 4793 perovskite materials with a general formula of A_{1-x}A'_xB_{1-y}B'_yO₃ and includes a majority of the 2913 materials analyzed by Jacobs et al. [²⁵] and Ma et al. [²⁷] as well as binary materials (ABO₃) taken from the Materials Project database. The composition of all the materials used in the present study are provided in the Excel spreadsheet as Supporting Information. Here, we used four successive filters to eliminate materials that do not satisfy the requirements for effective PCCs. In the first stage (Filter 1), the bandgap is used as elimination criterion and materials exhibiting a bandgap less than 2.0 eV were eliminated from the dataset. A bandgap greater than 2.0 eV was selected to isolate compounds that are strongly insulating and suitable for electrolyte applications. The next three filters focused on

identifying the materials that are stable under anodic oxidizing conditions (Filter 2), cathodic reducing conditions (Filter 3), and in the presence of CO₂ (Filter 4). The stability was determined from the energy above the convex hull of the phase diagram made from the constituent elements. A cutoff value of 40 meV/atom for E_{hull} was chosen to account for the uncertainty range of a typical DFT calculation and any material exhibiting an E_{hull} > 40 meV/atom for each filter were eliminated successively [40,41]. We used the phase stability analysis tools in Pymatgen to compute multicomponent grand potential phase diagrams [42,43]. All stability calculations were carried out under SOFC operating conditions at a typical intermediate temperature of 1073 K where the anode and cathode are open to H₂ and O₂ gas, respectively. For stability under a CO₂ environment (Filter 4), the calculations were carried out in a system open to both O₂ and CO₂. The chemical potentials of the gas molecules were calculated at typical SOFC conditions of $p(H_2) = 1$ atm and $p(H_2O) = 0.03$ atm for anode stability [11,44], $p(O_2) = 0.21$ atm and relative humidity of 30% for cathode stability [25,45], and 1 ppb CO and p(CO₂) = 1.00 atm for CO₂ stability [46]. Full details of these stability calculations can be found in Section S2 of the Supporting Information.

155

156

157

158

159

160

161

162

163

164

165

166

167

168

169

170

171

172

173

174

175

176

Next, we evaluated the ability to form an oxygen vacancy and protonic defects for the materials that passed the first three elimination criteria. The stability of a charge-neutral vacancy defect (V_0^{\times} in Kröger-Vink notation [47]) was examined by creating an oxygen vacancy with a stoichiometry of ABO_{3- δ} (δ = 0.125). All non-identical positions in the 40-atom supercell with 24 oxygen atoms were tested. For creating a charge-neutral protonic defect (OH^{\times}), a single proton is added to the oxygen that was identified as the minimum energy vacancy formation site. The defect structures were optimized using the same lattice vectors as the defect free cell. The

defect formation energy (ΔE_f) for charge neutral defects is calculated utilizing the following equation [⁴⁸]:

$$\Delta E_f = E_{defect} - E_{pristine} + \sum_i n_i \mu_i \tag{1}$$

where E_{defect} and E_{pristine} correspond to the SCF energies of the relaxed supercells in the presence and absence of a defect, respectively, n_i being the number of defect atoms removed or added to the pristine supercell, and μ_i being the chemical potential of the defect atom. We conduct defect formation analysis at 0 K, and therefore, the chemical potentials of O and H are equivalent to E_O and E_H , respectively. E_O and E_H are defined with the following equations:

$$E_O = \frac{E_{O_2}}{2} \tag{2}$$

$$E_H = \frac{E_{H_2O} - E_O}{2} \tag{3}$$

 E_{O_2} and E_{H_2O} are equal to the 0 K energies for oxygen and water, respectively. We calculated the hydration energy utilizing the following equation [29,49]:

$$\Delta E_{hydr} = 2\Delta E_{f,OH_O^{\times}} - \Delta E_{f,V_O^{\times}}$$
 (4)

 $\Delta E_{f,V_O^{\times}}$ is the charge-neutral formation of an oxygen vacancy and $\Delta E_{f,OH_O^{\times}}$ is the charge-neutral proton insertion energy. A detailed discussion regarding the calculations of defect formation energies and the derivation of ΔE_{hvdr} is provided in Section S1 of the Supporting Information.

3. Results and Discussion

3.1.1 Filter 1 – Electronic Conductivity

One of the key requirements for an electrolyte material is that it should exhibit high ionic conductivity and at the same time high resistance towards electronic conductivity. Hence, we chose electronic conductivity as our first elimination criterion (Filter 1) and set a bandgap limit of 2.0 eV to isolate compounds that are strongly insulating. Calculated bandgaps for all the 4793

materials at GGA-level (GGA+U-level for V, Cr, Mn, Fe, Co, Ni containing compositions) are provided in the Excel spreadsheet as Supporting Information. As displayed under Filter 1 in Figure 2, this filter eliminates 3,887 materials that exhibit a bandgap lower than 2.0 eV and the remaining 906 perovskites are considered for further screening. It is to be noted that the electrical conductivity analysis is done at 0 K and without considering any off-stoichiometry effects. Temperature effects such as magnetic transitions or structural changes are considered out-ofscope for this first-pass screening. A-site elemental analysis of the 906 passing compositions as displayed in Figure S6(a) of the Supporting Information indicates that the alkaline earth metals Ba and Sr are the dominant A-site elements that are included in compounds that exhibit bandgaps > 2.0 eV. Secondary dominant A-site elements include alkaline earth Ca, group 3 element Y, and the lanthanides La and Pr. The B-site elemental analysis is illustrated in Figure S6(b) which suggests that the majority of the passing materials have Zr as a B-site element and Ce being the second dominant B-site element. Transition metals such as Co, Cr, Fe, and Ni and p-block elements such as Ga, P, and Sb are the next prominent B-site elements of the identified insulating configurations.

199

200

201

202

203

204

205

206

207

208

209

210

211

212

213

214

215

216

217

218

219

220

221

3.1.2 Filter 2 – Thermodynamic Stability Under Anode Operating Conditions

The second elimination criterion (Filter 2) focuses on excluding materials that are not stable under typical anode operating conditions (T = 1073 K, $p(H_2) = 1 \text{ atm}$, and $p(H_2O) = 0.03 \text{ atm}$). The energy above the convex hull (E_{hull}) at anode operating conditions was calculated for all the perovskite materials and we eliminated the materials with E_{hull} values above 0.041 eV/atom. E_{hull} acts as a measure of the decomposition energy for a material and a value of $E_{hull} = 0 \text{ means}$ the configuration is formally stable and on the convex hull. As explained earlier in Section 2, the cutoff value of 0.041 eV/atom was chosen to account for the uncertainty range (40)

meV/atom) of a typical DFT calculation [^{40,41,50}] and in addition, a similar value has been used in the literature for material metastability analysis in SOFC applications [²⁵]. This analysis eliminated 781 materials and we identified 125 perovskites that are both insulators and stable under anode operating conditions.

Further elemental analysis revealed that the materials with the following elements at the A-site, Be, Dy, Gd, Ho, Nd, Sm, and Y, were found to be unstable under anode conditions. Most of these elements are lanthanides except for the alkaline earth Be and group 3 element Y. Additionally, materials with the following B-site elements, Al, Cu, Mg, Mo, Ni, P, Pr, Re, Rh, Sb, and Zn, exhibited instability under anode operating conditions. The elemental analysis of the passing configurations is plotted in Figure S7 of the Supporting Information. The primary A-site elements (Figure S7(a)) of the passing configurations remain Ba and Sr as identified in the case of electronic conductivity analysis (Figure S6(a)) and Ca, Cs, La, and Rb being the prominent minority elements. Similarly, the dominant B-site element of the passing configurations remains Zr (Figure S7(b)) with Ce, Hf, Sc, Sn, and Ti as the prominent minority elements. Transition metals Cr and Fe and group 5 metals Nb, V, and Ta, all appear in at least four of the passing configurations.

3.1.3 Filter 3 – Thermodynamic Stability Under Cathode Operating Conditions

The next filter (Filter 3) focuses on identifying materials that are stable under typical cathode operating conditions of T = 1073 K, $p(O_2) = 0.21$ atm, and a relative humidity of 30%. We computed the energy above the convex hull for all materials under cathode operating conditions as displayed in the Excel spreadsheet of the Supporting Information. Among the 125 perovskites identified from Filter 2, 9 materials were found to be unstable ($E_{hull} > 40$ meV/atom) under cathode operating conditions and thus eliminated from the data set. The materials that

were found to be unstable under cathode operating conditions are, Ba_{0.875}Sn_{0.125}ZrO₃, $Ba_{0.75}Sn_{0.25}ZrO_3$, $Sr_{0.75}Ca_{0.25}Zr_{0.75}V_{0.25}O_3$, $La_{0.5}Ca_{0.5}Zr_{0.75}Fe_{0.25}O_3$, $Pr_{0.5}Sr_{0.5}Zr_{0.75}Fe_{0.25}O_3$, $Y_{0.5}Ca_{0.5}Zr_{0.75}Fe_{0.25}O_3$, $Y_{0.5}Ca_{0.5}Zr_{0.75}Mn_{0.25}O_3$, BaNb_{0.5}Cr_{0.5}O₃, and SrZr_{0.75}Re_{0.25}O₃. Further analysis indicated that the A-site elements, Pr and Sn, and B-site element Re are completely eliminated from the passing configurations. The 116 perovskite materials that passed these first 3 filters are listed in Table S2 and the elemental analysis of these passing configurations are plotted in Figure S8 of the Supporting Information. As observed earlier, Ba and Sr remain the dominant A-site elements and Zr is the dominant B-site element in these passing configurations. Next, we identified 15 configurations (Table S3) that are stable under anodic and cathodic conditions but yield a bandgap between 1.0 and 2.0 eV. These materials could be potential candidates for electrolyte applications, but we did not conduct oxygen vacancy and hydration analysis on these materials. The elemental composition of these configurations includes mixed A-sites composed of Ba, Ca, Sr, and Rb; and mainly a Zr majority B-site doped with Mn, Cr, V, Os, Rh, and Ru. Two unique configurations that do not include Zr are Ba_{0.5}Rb_{0.5}Ce_{0.5}Nb_{0.5}O₃ and $Ba_{0.5}Rb_{0.5}Ce_{0.5}Ta_{0.5}O_3$.

245

246

247

248

249

250

251

252

253

254

255

256

257

258

259

260

261

262

263

264

265

266

267

In agreement with the earlier report by Islam et. al. [29], we find that Zr and V (and group 5 elements Nb and Ta) configurations generally are water stable. Our calculations also predicted good stability for Ti-containing configurations under humid conditions which contradicts the observation by these authors. Most Co- and Ni-containing materials were eliminated based on their instability under anode operating conditions. Cr, Fe, Tc, and Zn are the primary high group number d-block elements that are present in the materials passing Filter 3. We note here that the benchmarking PCCs, BCO and BZO are also included in the list of materials passing the first 3 filters which further suggests that our calculations are consistent with the experimentally

observed stability of these materials [12] as discussed in Section S3.2 of the Supporting Information.

3.1.4 Filter 4 – Thermodynamic Stability Under CO₂ environment

268

269

270

271

272

273

274

275

276

277

278

279

280

281

282

283

284

285

286

287

288

289

One of the main drawbacks of BCO-based electrolytes is known to be the material instability in the presence of CO₂. Hence, we examined the thermodynamic stability of the perovskite materials in our data set under a CO₂ environment (T = 1073 K, 1 ppb CO, and $p(CO_2) = 1.00$ atm) by calculating the energy above the convex hull. This screening step (Filter 4) eliminates another 73 materials from the data set of 116 materials identified from Filter 3 leaving only 43 materials (Table 1) that are stable under a wide range of environmental conditions and also exhibit high electronic resistivity. We note that BZO passes all the four filters in agreement with experimental observation [51,52]. Other passing binary perovskite oxides include SrZrO₃ and YCrO₃. Overall, Ba (A-site) and Zr (B-site) are the predominant elements in the 43 configurations that passed all the four filters and Ce was eliminated completely from the list after the CO₂ stability test. Other prominent alkaline earth A-site elements include Sr and Ca that are present in 24 and 7 configurations, respectively. Non-alkaline earth A-site elements including Cd, Rb, and Zn are also present in these configurations but only at low concentrations (e.g., 12.5%). Other prominent B-site elements include Hf, Sn, and Ti which are present in 6, 5, and 6 configurations, respectively. The presence of Zr, Hf and Ti in the passing configurations suggests that the presence of group 4 elements at the B-site could improve stability in the presence of CO₂ and water-containing conditions. Lastly, the transition metal Fe is present in 3 configurations and these configurations include more unique elements such as Bi and the group 5 metals, Nb and Ta.

 $\begin{tabular}{ll} \textbf{Table 1:} List of materials that passed the four filters described in Figure 2. Included in this table are the elemental configuration, the computed bandgap (in eV), vacancy formation energy (ΔE_{vac} in eV), and hydration energy (ΔE_{hydr} in eV). \end{tabular}$

Α			A'	B		В'		B"		Bandgap (eV)	ΔE _{vac} (eV)	ΔE _{hydr} (eV)
Ва	1.000			Zr	1.000					3.329	6.757	-0.073
Sr	1.000			Zr	1.000					3.856	6.849	0.282
Υ	1.000			Cr	1.000					3.847	5.737	0.461
Ва	1.000			Zr	0.875	Pt	0.125			2.043	2.924	1.530
Ва	1.000			Zr	0.875	Sn	0.125			3.468	4.658	2.309
Ва	1.000			Zr	0.875	Тс	0.125			2.285	5.381	-0.450
Ва	1.000			Zr	0.875	Ti	0.125			2.779	6.245	-0.909
Sr	1.000			Zr	0.875	Ge	0.125			3.861	4.901	0.793
Sr	1.000			Zr	0.875	Hf	0.125			3.818	6.643	0.025
Sr	1.000			Zr	0.875	Mn	0.125			3.169	3.186	-1.210
Sr	1.000			Zr	0.875	Sn	0.125			3.937	4.784	1.849
Sr	1.000			Zr	0.875	Ti	0.125			3.042	6.411	-0.852
Ва	1.000			Zr	0.750	Hf	0.125			3.366	6.771	0.012
Ва	1.000			Zr	0.750	Ir	0.125			2.149	4.024	-1.672
Ва	1.000			Zr	0.750	Hf	0.250			3.415	6.786	0.191
Ва	1.000			Zr	0.750	Ti	0.250			2.730	6.210	-1.233
Sr	1.000			Zr	0.750	Hf	0.250			3.805	6.646	0.163
Sr	1.000			Zr	0.750	Ti	0.250			3.120	6.392	-1.295
Ва	1.000			Zr	0.750	Sn	0.250			3.78	4.681	2.451
Sr	1.000			Zr	0.750	Sn	0.250			3.933	4.519	1.476
Ва	1.000			Zr	0.750	Nb	0.125	Fe	0.125	2.431	5.053	-2.039
Ва	1.000			Zr	0.750	Та	0.125	Fe	0.125	2.808	5.327	-2.281
Ва	1.000			Zr	0.500	Hf	0.500			3.520	6.843	0.368
Sr	1.000			Zr	0.500	Hf	0.500			3.936	6.86	0.492
Ва	0.875	Ca	0.125	Zr	1.000					3.396	6.686	-0.313
Ва	0.875	Cd	0.125	Zr	1.000					2.967	4.572	-1.382

Ва	0.875	Rb	0.125	Zr	1.000				3.377	3.583	-3.859
Ва	0.875	Sr	0.125	Zr	1.000				3.350	6.721	-0.131
Sr	0.875	Ва	0.125	Zr	1.000				3.775	6.783	0.179
Sr	0.875	Ca	0.125	Zr	1.000				3.881	6.813	0.105
Sr	0.875	Zn	0.125	Zr	1.000				3.838	5.189	-0.395
Ва	0.875	Sr	0.125	Zr	0.875	Ti	0.125		2.930	6.253	-0.842
Sr	0.875	Ва	0.125	Zr	0.875	Sn	0.125		3.866	4.682	1.913
Sr	0.875	Ca	0.125	Zr	0.875	Ti	0.125		3.147	6.369	-0.927
Ва	0.875	Bi	0.125	Zr	0.875	Fe	0.125		3.505	4.342	-1.687
Са	0.750	Ва	0.250	Zr	1.000				3.916	6.668	-0.041
Sr	0.750	Ва	0.250	Zr	1.000				3.445	6.272	-0.701
Са	0.750	Sr	0.250	Zr	1.000				3.999	6.117	-1.042
Sr	0.750	Ca	0.250	Zr	1.000				3.899	6.788	-0.149
Ва	0.750	Sr	0.250	Zr	1.000				3.363	6.697	-0.223
Sr	0.750	Rb	0.250	Zr	0.750	Та	0.250		3.296	6.282	-0.943
Ва	0.500	Sr	0.500	Zr	1.000				3.637	6.753	-0.040
Sr	0.500	Ca	0.500	Zr	1.000				4.034	6.792	0.341

3.2 Vacancy Formation and Hydration Energy Analysis

The ability to incorporate a high concentration of protons in the lattice is another key requirement for PCC electrolytes to achieve high proton conductivity. In perovskite oxides, this process occurs by the creation of an oxygen vacancy, which in general is promoted in the presence of an acceptor-dopant, and the hydration process at the vacancy site enables the proton incorporation. Hence, we calculated the oxygen vacancy formation and hydration energies for the 116 perovskite oxides that passed the first three filters. The calculated vacancy formation energies and hydration energies of these materials with respect to doping concentrations at A-and B-sites are displayed in Figures 3(a-d) with BCO and BZO as the benchmark materials. In

Figure 3(a), the materials are organized by the extent of A-site doping such that A_{1.0} refers to the non-doped configuration and A_{0.875}, A_{0.75}, and A_{0.5} correspond to the materials with 12.5%, 25%, and 50% doping at the A-site, respectively. Among the 116 materials, 55 materials have non-doped A-site configuration (A_{1.0}), 26 materials have the A_{0.75} configuration, and the A_{0.875} and A_{0.5} configurations were found in 25 and 10 materials, respectively. Figure 3(b) provides a magnified view around the benchmark BZO based on Figure 3(a). In Figure 3(c), the vacancy formation and hydration energies of the 116 materials are organized with respect to B-site doping, where B_{1.0} refers to a non-doped B-site material and B_{0.875}, B_{0.75}, and B_{0.5} correspond to the materials with 12.5%, 25%, and 50% doping at the B-site, respectively. Figure 3(d) provides a magnified view around the benchmark BZO based on Figure 3(c).

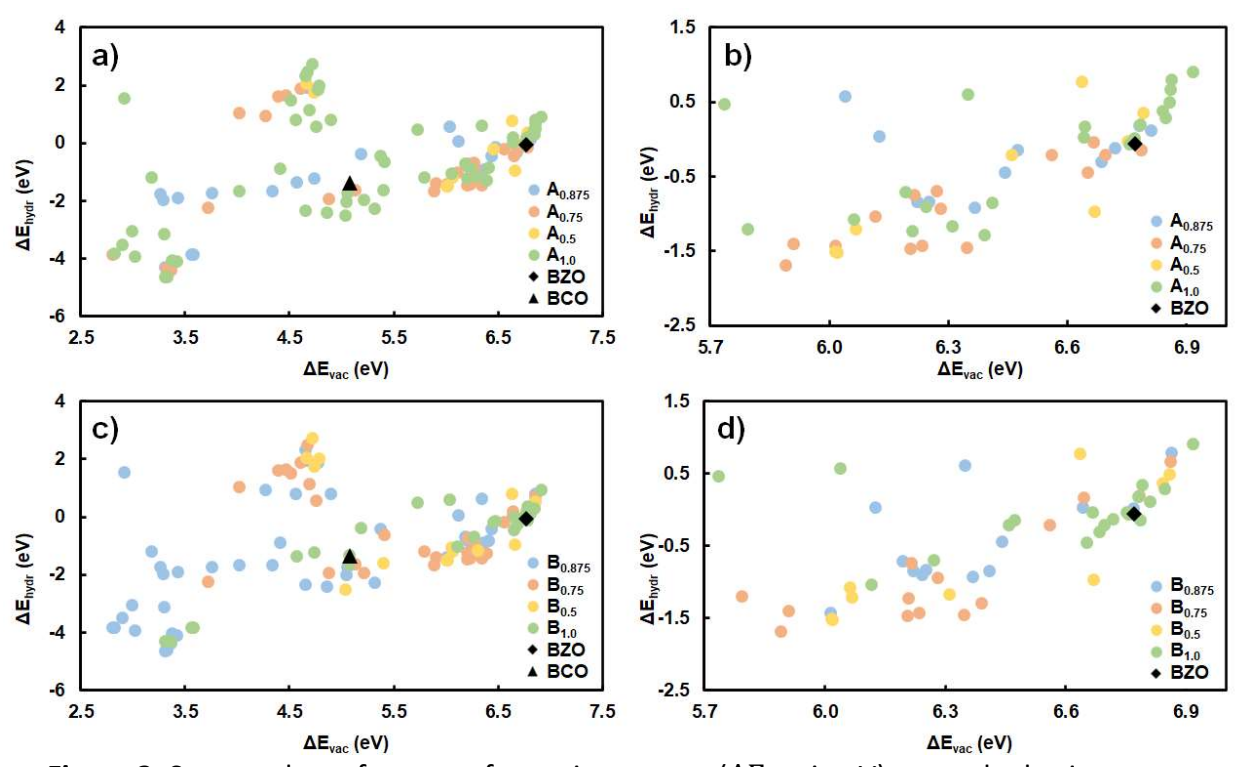


Figure 3: Scatter plots of vacancy formation energy (ΔE_{vac} in eV) verses hydration energy (ΔE_{hydr} in eV) for the 116 perovskite oxides that passed the first three filters. a) Materials organized with respect to A-site doping where A_{1.0}, A_{0.875}, A_{0.75}, and A_{0.5} correspond to the materials with 0%, 12.5%, 25%, and 50% doping at the A-site, respectively, b) magnified scatter plot around BZO taken from a), c) materials organized with respect to B-site doping where B_{1.0},

B_{0.875}, B_{0.75}, and B_{0.5} correspond to the materials with 0%, 12.5%, 25%, and 50% doping at the B-site, respectively, and d) magnified scatter plot around BZO taken from c).

Four different regions are identified in Figure 3(a) and (c) that can be classified as, the 310 Sn-containing region ($\Delta E_{vac} = 4.3 - 5.0 \text{ eV}$, $\Delta E_{hvdr} = 1.0 - 3.0 \text{ eV}$), the acceptor-dopant region 311 $(\Delta E_{vac} = 2.7 - 3.5 \text{ eV}, \Delta E_{hydr} = -5.0 - -3.0 \text{ eV})$, the BCO-like region $(\Delta E_{vac} = 4.5 - 5.5 \text{ eV},$ 312 $\Delta E_{hvdr} = -2.0 - 1.0 \text{ eV}$), and the BZO-like region ($\Delta E_{vac} = 6.0 - 7.0 \text{ eV}$, $\Delta E_{hvdr} = -1.0 - 1.0$ 313 eV). A linear-like relationship spans across the three regions including the acceptor-dopant, 314 BCO-like, and BZO-like regions. 70.7 % of A-site doped (e.g., A_{0.875}, A_{0.75}, and A_{0.5}) materials 315 and 69.0 % of B-site doped (e.g., B_{0.875}, B_{0.75}, and B_{0.5}) materials exhibit oxygen vacancy 316 formation energy values below 5.5 eV. Figure 3(b) displays all configurations located near the 317 BZO-like region displaying a mixture of $A_{1.0}$, $A_{0.875}$, $A_{0.75}$, and $A_{0.5}$ materials with an $A_{1.0}$ cluster 318 319 at higher oxygen vacancy defect and hydration energies relative to BZO. $A_{0.75}$ configurations primarily exhibit better vacancy formation (0.7 - 1.0 eV lower) and hydration activity (0.3 - 0.6 eV lower)320 eV lower) relative to BZO. Significant clustering of B_{1.0} materials occurs in the BZO-like region 321 322 with a small cluster in the acceptor-dopant region as displayed in Figures 3(c-d). In addition, a 323 prominent cluster was found around the acceptor-dopant region for the B_{0.875} configurations. B_{0.75} and B_{0.5} configurations cluster around the Sn-containing region and the intermediate zone 324 325 between the BCO-like and BZO-like regions, especially for vacancy formation energies between 326 5.8 and 6.4 eV. We note that the outlier A_{1.0} configuration, BaPt_{0.125}Zr_{0.875}O₃, located at the top 327 left corner of Figures 3(a) and 3(c) displays excellent vacancy formation activity (~ 3 eV) but has 328 Sn-like hydration activity ($\sim 2 \text{ eV}$).

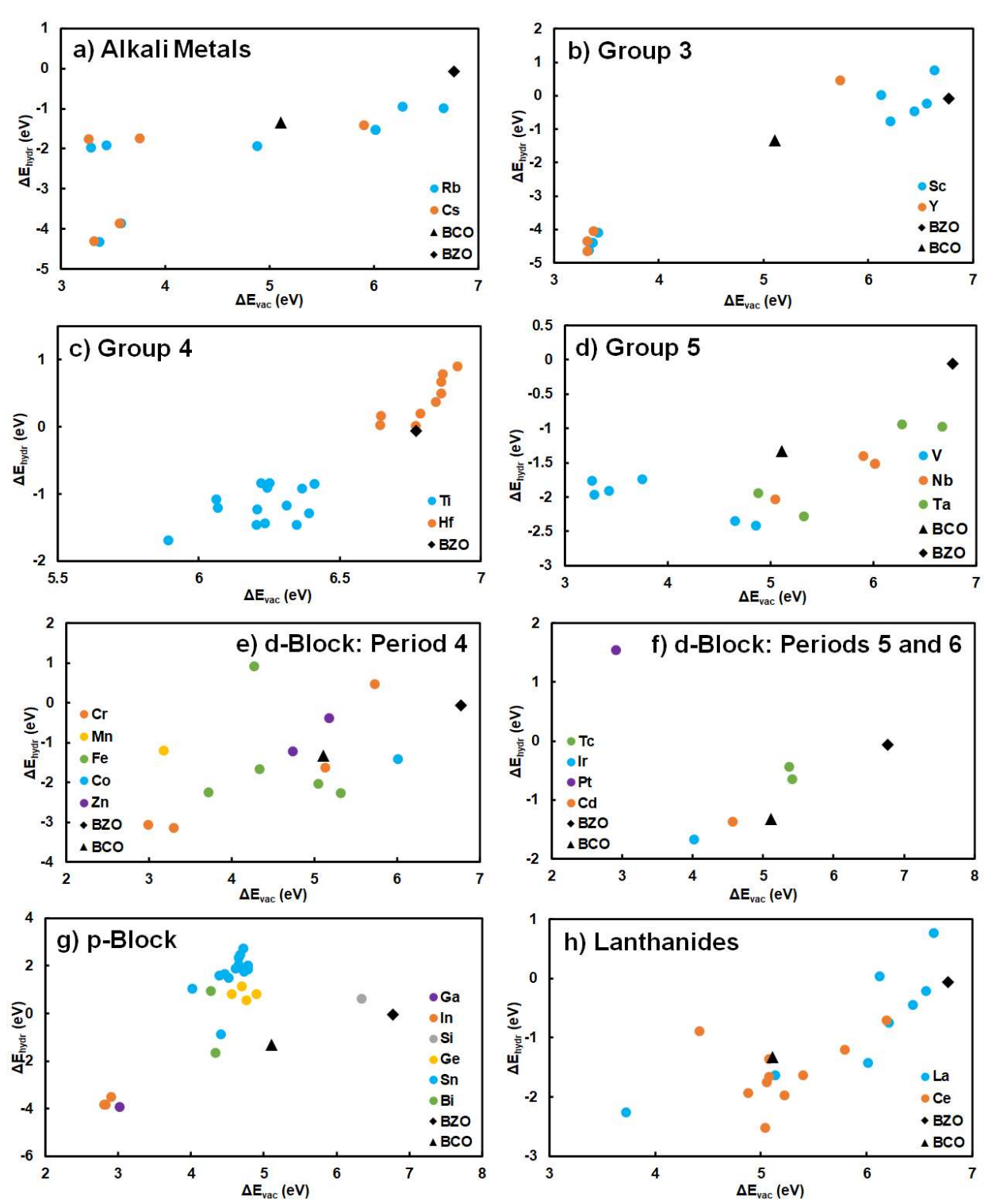


Figure 4: Scatter plots of vacancy formation energy (ΔE_{vac} in eV) verses hydration energy (ΔE_{hydr} in eV) for the 116 perovskite oxides that passed the first three filters categorized into the following groups, (a) alkali metals, (b) group 3 elements, (c) group 4 elements, (d) group 5 elements, (e) d-block: period 4 elements, (f) d-block: periods 5 and 6 elements, (g) p-block elements, and (h) lanthanides.

Next, we analyzed the role of various elements in determining the oxygen vacancy formation and hydration activity for the 116 perovskites by categorizing them into different groups as displayed in Figure 4. As discussed earlier, materials with acceptor-dopant elements exhibit good activity for both vacancy formation and the hydration process and most of these materials have A_{1.0} and B_{0.875} configurations (e.g., Figures 3(a) & 3(c)). Other materials that fall into this category are Cs_{0.125}Ba_{0.875}ZrO₃, Rb_{0.125}Ba_{0.875}ZrO₃, Cs_{0.125}Sr_{0.875}ZrO₃, Rb_{0.125}Sr_{0.875}ZrO₃, $Sr_{0.25}Ba_{0.75}In_{0.125}Zr_{0.875}O_3$, $Sr_{0.25}Ba_{0.75}Sc_{0.125}Zr_{0.875}O_3$, $Sr_{0.25}Ba_{0.75}Y_{0.125}Zr_{0.875}O_3$, and La_{0.25}Sr_{0.75}Sc_{0.25}Zr_{0.75}O₃. The categorized scattered plots in Figure 4 suggest that the materials fall into this acceptor-doped region have either alkali metals doping the A-site (Figure 4(a)), or group 3 (Figure 4(b)) and group 13 (Figure 4(g)) elements doping the B-site. Figure 4(a) further suggests that in addition to the high activity regime the alkali metals also exhibit another regime with stagnant hydration activity across a range of vacancy formation energy. High defect formation activity occurs with an A-site doping ratio of 12.5% and a non-doped Zr B-site backbone. The introduction of a small percentage of the 1⁺-ion at the A-site oxidizes Zr such that hydration becomes favorable upon Zr reduction. For BCO-like alkali metal-containing configurations, B-site doping with group 5 elements (mostly V, Figure 4(d)) can also alter the oxidation state of Zr during vacancy formation and hydration processes. B-site doping with group 3 elements (Sc and Y, Figure 4(b)) also displays two regions of activity, the acceptordopant region and BZO-like region. The materials at the acceptor-dopant region are composed of an alkaline earth metal at the A-site and Zr at the B-site doped with 12.5% of a group 3 metal. Here, the acceptor-dopants, Sc^{3+} or Y^{3+} enable creation of oxygen vacancies which promotes the hydration process. Our results are consistent with experimental observations that acceptor-doped perovskites such as Y-doped BaZrO₃ (BZY) conformers are stable and display ionic conductivity

329

330

331

332

333

334

335

336

337

338

339

340

341

342

343

344

345

346

347

348

349

350

[9,53]. This acceptor-dopant activity was also observed for group 13 elements (Ga and In) as displayed in Figure 4(g). These elements are more active for vacancy formation but exhibit approximately 0.3 – 0.5 eV higher hydration energies relative to group 3 elements. Among the dblock elements, only Cr falls into this acceptor-dopant region when it is present in small concentrations (e.g., 12.5%) on the B-site as displayed in the bottom-left of Figure 4(e). This analysis suggests that doping the A-site with alkali metals or doping the B-site with both groups 3 and 13 elements can improve both the vacancy formation and hydration activities of the PCC materials. We note that BZY conformers are in general affected by the acceptor-dopant trapping effect where large proton rotation barriers isolate proton transportation to other oxygen sites in the material [54]. Previous DFT studies outlined that Rb- and Cs-containing BZO conformers display a localized or weaker proton trapping and similar proton migration barriers to BZY conformers [19,55]. Examination of this effect on proton migration barriers (e.g., migration and transportation) is considered out-of-scope for this study (see Section S3.3 of the Supporting Information).

Materials that have B-site doping with the p-block elements (Sn, Ge, and Bi; Figure 4(g)) fall into the Sn-containing region which exhibit slightly lower oxygen vacancy formation energies but higher hydration energies relative to BCO. Whereas, doping with lanthanides (mostly Ce, Figure 4(h)) results in a similar vacancy formation activity but better hydration activity compared to BCO. Bader charge analysis provided in Table S4 of the Supporting Information suggests that Ce⁴⁺ is reduced to Ce³⁺ and re-oxidized to Ce⁴⁺ during vacancy formation and hydration processes, respectively, and thus, the hydration activity is promoted on Ce-containing materials. On the other hand, Sn is reduced from a 4⁺ to a 2⁺ state during the vacancy formation process and partially oxidizes back to the unfavorable 3⁺ state during the

hydration process. Therefore, materials with these group 14 elements exhibit a reasonable vacancy formation activity but lower hydration activity. Previous experimental [⁵⁶] and DFT [⁵⁷] studies have shown Sn is an effective dopant when co-doped with an acceptor-dopant Y in BZO to form BSYZ. BSYZ displays good stability and ionic conductivity but is affected by the proton trapping effect at high Y concentrations [²⁰].

375

376

377

378

379

380

381

382

383

384

385

386

387

388

389

390

391

392

393

394

395

396

The perovskite oxides in the BCO-like region display intermediate vacancy formation and hydration energies and most of these materials are composed of A_{1.0} configuration with mixed B-site doping ratios of 12.5%, 25%, and 50% (Figures 3(a) & 3(c)). In addition to the Cecontaining lanthanide configurations (Figure 4(h)) discussed above, the materials in the BCOlike region are composed of an alkali metal Rb (Figure 4(a)), group 5 elements V, Nb, and Ta (Figure 4(d)), and d-block elements Fe, Cr, Cd, and Zn (Figures 4(e) & 4(f)). The alkali metalcontaining configuration in the BCO-like region, Rb_{0.25}Ba_{0.75}Ta_{0.25}Ce_{0.75}O₃ is free of Zr and is composed of Ce and the group 5 element Ta at the B-site, and therefore, this is a promising configuration for CO₂-free conditions as lower sintering temperatures are expected. All other configurations with group 5 and d-block elements do not contain Ce. Regarding configurations containing d-block elements that can readily adopt multiple oxidation states, three Fe-containing oxides, $BaFe_{0.125}Ta_{0.125}Zr_{0.875}O_3$, $BaFe_{0.125}Nb_{0.125}Zr_{0.875}O_3$, and $Bi_{0.125}Ba_{0.875}Fe_{0.125}Zr_{0.875}O_3$, the Co-containing oxide La_{0.25}Ba_{0.75}Co_{0.125}Zr_{0.875}O₃ and the Cr-containing configuration, La_{0.25}Sr_{0.75} Cr_{0.25}Zr_{0.75}O₃ exhibit hydration energies similar to BCO. The Ce-containing configurations (Figure 4(h)) have a general stoichiometry of A²⁺Zr_xCe_{1-x}O₃. This is a classic strategy of mixing BZO and BCO without including the acceptor-dopant Y [52]. This analysis suggests that codoping the B-site with Fe and a group 5 element could yield BCO-like defect formation activity.

The perovskite oxides in the BZO-like region display intermediate hydration energies but high vacancy formation energies (Figure 3(a)). Many of these configurations have co-doped alkaline earth elements such as Sr and Ba at the A-site and Zr-containing configurations that are co-doped with other group 4 elements such as Ti and Hf at the B-site. Among the group 4 elements, materials with Ti dopant exhibit better vacancy formation and hydration activity relative to BZO, whereas Hf-containing configurations exhibit similar or less activity than BZO (Figure 4(c)). A couple of other materials in the BZO-like region contain alkali metals at high concentrations (50%) at the A-site together with group 5 metals at high concentrations (50%) at the B-site and exhibit slightly better hydration activity than BZO (Figures 4(a) & 4(d)). Most of the La-containing configurations in the BZO-like region also have the group 3 element Sc in the B-site at low doping ratios (12.5 - 25%) and exhibit slightly better vacancy formation activity than BZO (Figures 4(b) & 4(h)). Materials with d-block elements do not appear in the BZO-like region, whereas one configuration with the p-block element Si has similar activity as BZO (Figure 4(e)). Analysis of this region mainly suggests that doping with Ti can improve the activity relative to BZO.

397

398

399

400

401

402

403

404

405

406

407

408

409

410

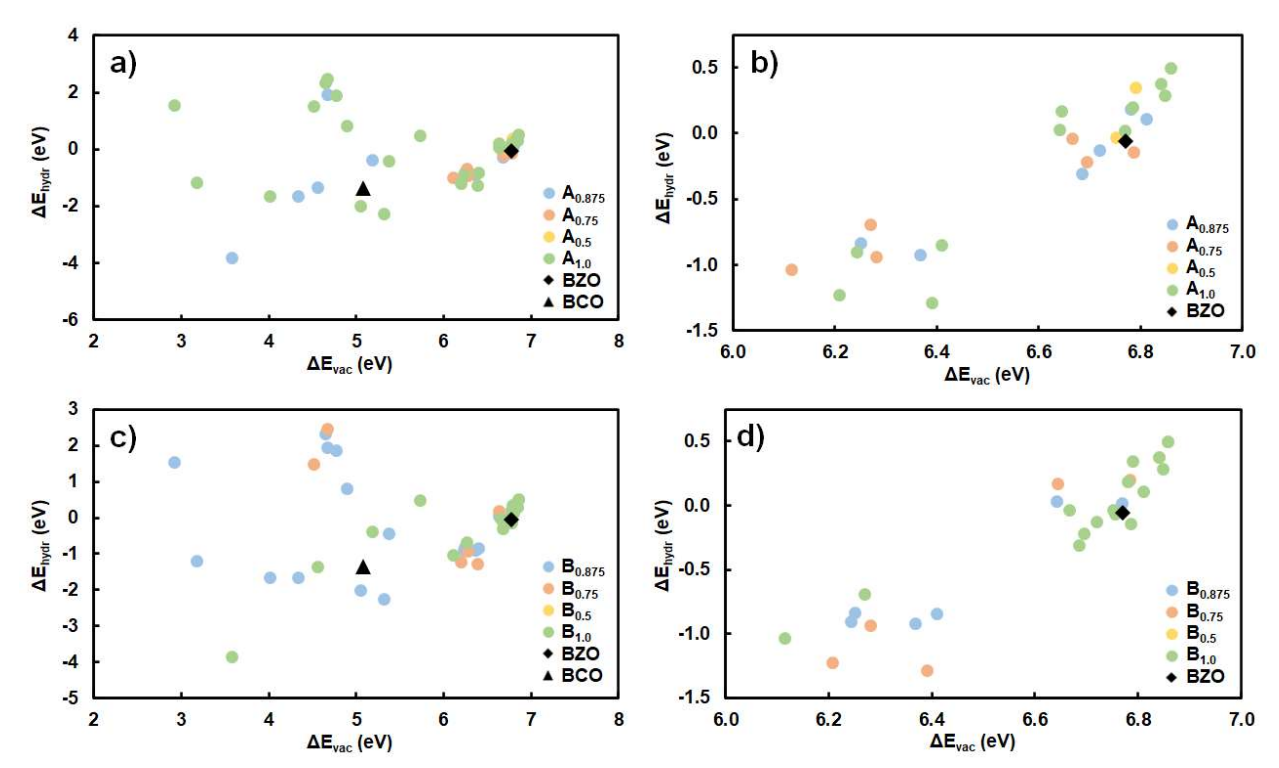


Figure 5: Scatter plots of vacancy formation energy (ΔE_{vac} in eV) verses hydration energy (ΔE_{hydr} in eV) for the 43 perovskite oxides that passed the first four filters. a) Materials organized with respect to A-site doping where A_{1.0}, A_{0.875}, A_{0.75}, and A_{0.5} correspond to the materials with 0%, 12.5%, 25%, and 50% doping at the A-site, respectively, b) magnified scatter plot around BZO taken from a), c) materials organized with respect to B-site doping where B_{1.0}, B_{0.875}, B_{0.75}, and B_{0.5} correspond to the materials with 0%, 12.5%, 25%, and 50% doping at the B-site, respectively, and d) magnified scatter plot around BZO taken from d). BCO did not pass the CO₂ stability test and is included in the figure only as a benchmark.

Figure 5 displays the vacancy formation and hydration energies of the 43 configurations (Table 1) that passed all the four filters including the CO_2 stability test and are categorized with respect to A- and B-site doping ratios. We note here that the application of Filter 4 eliminates all materials in the acceptor-dopant region ($\Delta E_{vac} = 2.7 - 3.5 \text{ eV}$, $\Delta E_{hydr} = -5.0 - -3.0 \text{ eV}$; Figure 3), except for $Ba_{0.875}Rb_{0.125}ZrO_3$, suggesting that these materials are not stable under a 1 atm CO_2 environment. Only two configurations, $BaPt_{0.125}Zr_{0.875}O_3$ and $SrMn_{0.125}Zr_{0.875}O_3$, exhibit vacancy formation energies (2.9 - 3.2 eV) similar to that of acceptor-dopant materials, however, the hydration energies (-1.2 - 1.5 eV) are in the range of BCO-like or Sn-containing materials.

While BCO itself did not pass the CO₂ stability test, other materials in the BCO-like region that exhibit similar or better vacancy formation and hydration activity are: BaFe_{0.125}Ta_{0.125}Zr_{0.875}O₃, $BaFe_{0.125}Nb_{0.125}Zr_{0.875}O_3$, $Bi_{0.125}Ba_{0.875}Fe_{0.125}Zr_{0.875}O_3$, $BaRb_{0.125}Zr_{0.875}O_3$, $BaCd_{0.125}Zr_{0.875}O_3$, and BaIr_{0.125}Zr_{0.875}O₃. In the Supporting Information, Figure S9 displays the hydration energy verses vacancy formation energy for all the 116 materials that passed the first three filters and organized with respect to their stability under CO₂ environment. This figure clearly shows that most materials in the better defect formation activity region ($\Delta E_{vac} < 5~eV$ and $\Delta E_{hydr} <$ -1.5 eV) are either metastable ($E_{hull} = 0.041-0.081 \text{ eV/atom}$) or unstable ($E_{hull} > 0.081 \text{ eV/atom}$) in the presence of CO₂. The metastable materials may be suitable for low pressure CO₂ (e.g., p(CO₂) < 1.00 atm) applications and are listed in Table S5. Among these metastable materials, notable Cefree materials that are BCO-like include the following: Rb_{0.125}Ba_{0.875}V_{0.125}Zr_{0.875}O₃, containing) configurations, Jeong et. al. used DFT calculations to show that significant proton trapping affects Zn-doped BZO limiting its practical applicability [58]. Overall, our analysis suggests that A-site doping with low concentration of an alkali metal complimented with low concentration group 5 metal doping at the B-site is an effective strategy to generate thermodynamically stable perovskite-based PCCs that are strongly insulating and adequate ionic conductors.

3.3 Secondary Filtering for Electrode Materials

420

421

422

423

424

425

426

427

428

429

430

431

432

433

434

435

436

437

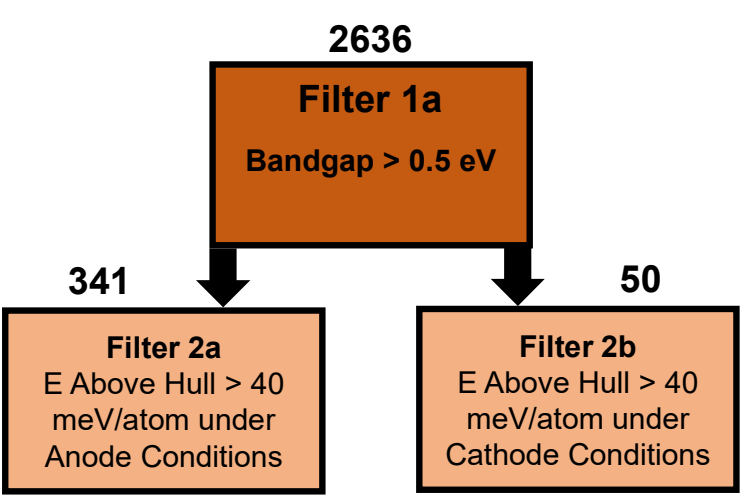


Figure 6: DFT-based high-throughput screening process used for identifying electrode materials. The number above each filter box refers to the number of materials that pass the corresponding filter criterion.

A secondary screening process used to propose materials that could have potential use for electrode applications is described in Figure 6. Since electrode materials should exhibit good electronic conductivity, our first elimination criterion (Filter 1a) focuses on identifying materials that exhibit smaller bandgap (< 0.5 eV) and we found 2636 materials out of the initial 4793 data set satisfy this criterion. These materials are further tested for stability under anode (Filter 2a) and cathode (Filter 2b) operating conditions as explained earlier for PCC materials screening. We found 341 materials that passed the anode stability test and only 50 materials passed the cathode stability test and could have potential use as an anode and cathode, respectively. The materials identified under different categories are listed in the Excel spreadsheet as Supporting Information. We did not perform any secondary analysis such as vacancy formation or ionic conductivity on these set of materials as this is considered out-of-scope for this study.

Next, we examined the elemental composition of configurations that are electrically active (e.g., Filter 1a passing) in Figure S10. For the A-site, the alkaline earth elements Ba and Sr are the most common elements with frequencies both above one thousand and Ca being the third most common element. Like the electrically inactive results (e.g., Filter 1), lanthanides La and Pr

are the second most common elements. Group 3 element Y and other lanthanide elements such as Ce, Dy, Er, Gd, Nd, and Sm also occur at the A-site. A-site elements that pass Filter 1a but do not pass Filter 1 include lanthanides Ce and Er and alkali metals Li and Na. For the B-site, Fe and Zr are the most common elements followed by transition metals Co, Mn, and Ni, group 5 element Nb, and lanthanide Ce. Prominent B-site minority elements include group 5 elements Ta and V, group 15 elements P and Sb, and common 2⁺ elements such as Cu and Zn. B-site elements that pass Filter 1a but do not pass Filter 1 include Be, La, Os, Pd, Ru, and Sr. Lastly, in contrast to the electrically inactive results, configurations typically include low concentrations of Zr at the B-site.

4. Conclusions

In this study, we coupled first-principles materials science and a high-throughput screening methodology to analyze a wide variety of perovskite oxides for their potential use as proton conducting electrolyte materials. Starting from a data set of 4793 distinct perovskites with binary, tertiary, quaternary, and quinary compositions, our successive screening methodology focused on identifying materials that are strongly insulating, thermodynamically stable under various reaction environments, and have a better ability to incorporate protons. At each filtering stage we have analyzed the elemental identity and the role of A- and B-site doping in the passing materials such that the desirable macroscopic properties can be tuned for the specific applications. Elemental analysis of the 116 materials that passed the electronic conductivity and thermodynamic stability tests revealed that most of these materials possess Ba and Sr at the A-site with Zr being the dominant element at the B-site. Less dominant elements that appear in at least eight configurations are Ca, La, and Rb at the A-site and Ce, Hf, Sc, Sn, and Ti at the B-site. In terms of doping content, many of the promising materials possess a non-doped A-site

with Zr-containing B-site doped configurations. The second dominant configurations passing the stability tests include 12.5% and 25% doping at the A-site or 12.5% doping at the B-site suggesting that minimal doping is favorable for water stability. Our results are consistent with the experimental observation that the activity and stability of the state-of-the-art PCC material family based on Y-doped BZO is improved when the doping ratio is kept under 20% [59,60].

477

478

479

480

481

482

483

484

485

486

487

488

489

490

491

492

493

494

495

496

497

498

499

Oxygen vacancy formation and hydration energies of the 116 materials were calculated as a measure of their ability to incorporate protons and the materials were categorized into four regions based on their activity. Materials that fall into the acceptor-dopant region exhibit high activity for both vacancy formation and hydration processes and many of these materials have either alkali metal doped A-sites or B-sites doped with both groups 3 and 13 elements. A second set of materials identified in the Sn-containing region exhibit reasonable vacancy formation activity, but lower hydration activity and these materials mainly have B-sites doped with the pblock elements such as Sn, Ge, and Bi. The third region around the benchmark material BCO consists of materials exhibiting intermediate vacancy formation and hydration energies and most of these materials have non-doped A-site configuration with mixed B-site doping ratios of 12.5%, 25%, and 50%. A fourth region includes configurations with an A-site co-doped with alkaline earth metals and a non-doped Zr B-site that behave similarly to the BZO benchmark material and exhibit poor activity for both vacancy formation and hydration processes. Although the materials in the acceptor-dopant region exhibit better defect formation activity, many of these materials are eliminated while applying the fourth filter that tests the stability under a CO₂ environment. The promising configurations identified from our high-throughput screening of PCC electrolytes that are strongly insulating, thermodynamically stable in the presence of H₂O and CO_2 (including borderline metastability under CO_2 with $E_{hull} < 0.08$ eV/atom) are:

 $BaFe_{0.125}Ta_{0.125}Zr_{0.875}O_3,\ BaFe_{0.125}Nb_{0.125}Zr_{0.875}O_3,\ Bi_{0.125}Ba_{0.875}Fe_{0.125}Zr_{0.875}O_3,\\ SrMn_{0.125}Zr_{0.875}O_3,\ BaRb_{0.125}Zr_{0.875}O_3,\ Rb_{0.125}Ba_{0.875}V_{0.125}Zr_{0.875}O_3,\ Rb_{0.125}Zr_{0.875}O_3,\ R$

In summary, this study serves to aid the fundamental understanding and principles for the design of perovskite-based proton conducting electrolytes. We elaborate on the role of elemental identity and doping ratios on thermodynamic stability and defect formation activity. Insights and guidelines obtained from this study could enable the selection of materials for various specific applications that require high electronic resistivity or good electronic conductivity, chemical stability against high oxidizing and reducing atmospheres and good proton incorporation ability. Future work will focus on testing a greater number of quaternary and quinary configurations and compute proton migration barriers to better understand the elemental role on the proton trapping effect.

Supporting Information

The Supporting Information is available free of charge via the Internet at http://pubs.acs.org.

Development of the perovskite material set, naming scheme, and schematic diagrams of
elemental arrangement for all doping ratios. Methodology for the free energies of all
gaseous species for phase analysis. Methodology of open phase diagrams with Pymatgen.
 Defect formation analysis and derivation of hydration energy formula. BZO and BCO
benchmark stability and defect formation analysis. Table of Filter 3 passing materials.

522	Figures of elemental frequency of passing materials for Filters 1-3 and Filter 1a. Bader					
523	analysis of Sn-containing configurations.					
524	• Excel spreadsheet that includes elemental configuration, bandgap size (eV), energy above					
525	the convex hull (eV/atom) for all environmental conditions, and defect formation analysis					
526	for Filter 3 passing materials.					
527						
528	Acknowledgments					
529	This work was supported by the National Science Foundation under Grant No. DMR- 1832809					
530	and partially supported by the South Carolina Smart State Center for Strategic Approaches to the					
531	Generation of Electricity (SAGE). Computing resources are provided by the U.S. Department of					
532	Energy facility located at National Energy Research Scientific Computing Center (NERSC)					
533	under Contract No. DE-AC02-05CH11231 and ACCESS facilities located at Texas Advanced					
534	Computing Center (TACC), San Diego Supercomputer Center (SDSC), and Purdue University					
535	(grand no. TG-CTS090100). Finally, computing resources provided by the University of South					
536	Carolina's High Performance Computing (HPC) group are gratefully acknowledged.					
537						
538	Author Information					
539	Corresponding Author					
540	*Email: heyden@cec.sc.edu					
541	Author Contributions					
542	All authors have given approval to the final version of the manuscript.					
543	Notes					
544	The authors declare no competing financial interest.					

References

545

556

557

558

559

560

561

562

563

564

565

566

567

568

569

570

- 546 (1) McIntosh, S.; Gorte, R. J. Direct Hydrocarbon Solid Oxide Fuel Cells. *Chem. Rev.*, **2004**, *104* (10), 4845–4866. https://doi.org/10.1021/cr020725g.
- 548 (2) Wachsman, E. D.; Lee, K. T. Lowering the Temperature of Solid Oxide Fuel Cells. 549 *Science*, **2011**, *334* (6058), 935–939. https://doi.org/10.1126/science.1204090.
- 550 (3) Ormerod, R. M. Solid Oxide Fuel Cells. *Chem. Soc. Rev.*, **2003**, *32* (1), 17–28. 551 https://doi.org/10.1039/b105764m.
- 552 (4) Steele, B. C. H.; Heinzel, A. Materials for Fuel-Cell Technologies. *Nature*, **2001**, 414 (6861), 345–352. https://doi.org/10.1038/35104620.
- 554 (5) Fergus, J. W. Electrolytes for Solid Oxide Fuel Cells. *J. Power Sources*, **2006**, *162* (1), 30–40. https://doi.org/10.1016/j.jpowsour.2006.06.062.
 - (6) Jaiswal, N.; Tanwar, K.; Suman, R.; Kumar, D.; Upadhyay, S.; Parkash, O. A Brief Review on Ceria Based Solid Electrolytes for Solid Oxide Fuel Cells. *J. Alloys Compd.*, 2019, 781, 984–1005. https://doi.org/10.1016/j.jallcom.2018.12.015.
 - (7) Gao, Z.; Mogni, L. v.; Miller, E. C.; Railsback, J. G.; Barnett, S. A. A Perspective on Low-Temperature Solid Oxide Fuel Cells. *Energy Environ. Sci.*, **2016**, *9* (5), 1602–1644. https://doi.org/10.1039/C5EE03858H.
 - (8) Hossain, S.; Abdalla, A. M.; Jamain, S. N. B.; Zaini, J. H.; Azad, A. K. A Review on Proton Conducting Electrolytes for Clean Energy and Intermediate Temperature-Solid Oxide Fuel Cells. *Renew. Sustain. Energy Rev.*, **2017**, *79*, 750–764. https://doi.org/10.1016/j.rser.2017.05.147.
 - (9) Fabbri, E.; Pergolesi, D.; Traversa, E. Materials Challenges toward Proton-Conducting Oxide Fuel Cells: A Critical Review. *Chem. Soc. Rev.* **2010**, *39* (11), 4355. https://doi.org/10.1039/b902343g.
 - (10) Fallah Vostakola, M.; Amini Horri, B. Progress in Material Development for Low-Temperature Solid Oxide Fuel Cells: A Review. *Energies*, **2021**, *14* (5), 1280. https://doi.org/10.3390/en14051280.
- 572 (11) Singh, K.; Kannan, R.; Thangadurai, V. Perspective of Perovskite-Type Oxides for 573 Proton Conducting Solid Oxide Fuel Cells. *Solid State Ion.*, **2019**, *339*, 114951. 574 https://doi.org/10.1016/j.ssi.2019.04.014.
- Tanner, C. W.; Virkar, A. v. Instability of BaCeO₃ in H2O -Containing
 Atmospheres. *J. Electrochem. Soc.*, **1996**, *143* (4), 1386–1389.
 https://doi.org/10.1149/1.1836647.
- 578 (13) Gregori, G.; Merkle, R.; Maier, J. Ion Conduction and Redistribution at Grain 579 Boundaries in Oxide Systems. *Prog. Mater. Sci.*, **2017**, *89*, 252–305. 580 https://doi.org/10.1016/j.pmatsci.2017.04.009.

- 581 (14) Gopalan, S.; Virkar, A. v. Thermodynamic Stabilities of SrCeO₃ and BaCeO₃ Using 582 a Molten Salt Method and Galvanic Cells. *J. Electrochem. Soc.*, **1993**, *140* (4), 583 1060–1065. https://doi.org/10.1149/1.2056197.
- Zuo, C.; Zha, S.; Liu, M.; Hatano, M.; Uchiyama, M. Ba(Zr_{0.1}Ce_{0.7}Y_{0.2})O_{3-δ} as an Electrolyte for Low-Temperature Solid-Oxide Fuel Cells. *Adv. Mat.*, **2006**, *18* (24), 3318–3320. https://doi.org/10.1002/adma.200601366.

588

589

590

591

592

593

594

595

596

597

598

599

600

601

602

605

606

- (16) Sawant, P.; Varma, S.; Wani, B. N.; Bharadwaj, S. R. Synthesis, Stability and Conductivity of BaCe_{0.8-x}Zr_xY_{0.2}O_{3-δ} as Electrolyte for Proton Conducting SOFC. *Int. J. Hydrog. Energy*, **2012**, *37* (4), 3848–3856. https://doi.org/10.1016/j.ijhydene.2011.04.106.
 - (17) Liu, Z.; Wang, X.; Liu, M.; Liu, J. Enhancing Sinterability and Electrochemical Properties of Ba(Zr_{0.1}Ce_{0.7}Y_{0.2})O_{3-δ} Proton Conducting Electrolyte for Solid Oxide Fuel Cells by Addition of NiO. *Int. J. Hydrog. Energy*, **2018**, *43* (29), 13501–13511. https://doi.org/10.1016/j.ijhydene.2018.05.089.
 - (18) Lyagaeva, J.; Antonov, B.; Dunyushkina, L.; Kuimov, V.; Medvedev, D.; Demin, A.; Tsiakaras, P. Acceptor Doping Effects on Microstructure, Thermal and Electrical Properties of Proton-Conducting BaCe_{0.5}Zr_{0.3}Ln_{0.2}O_{3-δ} (Ln = Yb, Gd, Sm, Nd, La or Y) Ceramics for Solid Oxide Fuel Cell Applications. *Electrochim. Acta*, 2016, 192, 80–88. https://doi.org/10.1016/j.electacta.2016.01.144.
 - (19) Løken, A.; Saeed, S. W.; Getz, M. N.; Liu, X.; Bjørheim, T. S. Alkali Metals as Efficient A-Site Acceptor Dopants in Proton Conducting BaZrO₃. *J. Mater. Chem. A.* **2016**, *4* (23), 9229–9235. https://doi.org/10.1039/c6ta01446a.
- 603 (20) Dawson, J. A.; Tanaka, I. Proton Trapping in y and Sn Co-Doped BaZrO₃. *J. Mater. Chem. A.* **2015**, *3* (18), 10045–10051. https://doi.org/10.1039/c5ta01450f.
 - (21) Zhou, Y.; Guan, X.; Zhou, H.; Ramadoss, K.; Adam, S.; Liu, H.; Lee, S.; Shi, J.; Tsuchiya, M.; Fong, D. D.; Ramanathan, S. Strongly Correlated Perovskite Fuel Cells. *Nature*, **2016**, *534* (7606), 231–234. https://doi.org/10.1038/nature17653.
- 608 (22) Nico, C.; Monteiro, T.; Graça, M. P. F. Niobium Oxides and Niobates Physical 609 Properties: Review and Prospects. *Prog. Mater. Sci.*, **2016**, *80*, 1–37. 610 https://doi.org/10.1016/j.pmatsci.2016.02.001.
- Zhao, L.; He, B.; Lin, B.; Ding, H.; Wang, S.; Ling, Y.; Peng, R.; Meng, G.; Liu, X.
 High Performance of Proton-Conducting Solid Oxide Fuel Cell with a Layered
 PrBaCo₂O_{5+δ} Cathode. J. Power Sources, 2009, 194 (2), 835–837.
 https://doi.org/10.1016/j.jpowsour.2009.06.010.
- Malavasi, L.; Fisher, C. A. J.; Islam, M. S. Oxide-Ion and Proton Conducting
 Electrolyte Materials for Clean Energy Applications: Structural and Mechanistic
 Features. *Chem. Soc. Rev.*, 2010, 39 (11), 4370–4387.
 https://doi.org/10.1039/b915141a.

- Jacobs, R.; Mayeshiba, T.; Booske, J.; Morgan, D. Material Discovery and Design
 Principles for Stable, High Activity Perovskite Cathodes for Solid Oxide Fuel
 Cells. Adv. Energy Mater., 2018, 8 (11). https://doi.org/10.1002/aenm.201702708.
- (26) Jacobs, R.; Liu, J.; Na, B. T.; Guan, B.; Yang, T.; Lee, S.; Hackett, G.; Kalapos, T.;
 Abernathy, H.; Morgan, D. Unconventional Highly Active and Stable Oxygen
 Reduction Catalysts Informed by Computational Design Strategies. *Adv. Energy Mater.*, 2022, *12* (25). https://doi.org/10.1002/aenm.202201203.
- 626 (27) Ma, T.; Jacobs, R.; Booske, J.; Morgan, D. Discovery and Engineering of Low 627 Work Function Perovskite Materials. *J. Mater. Chem. C*, **2021**, *9*, 12778–12790. 628 https://doi.org/10.1039/D1TC01286J.
- (28) Jacobs, R.; Luo, G.; Morgan, D. Materials Discovery of Stable and Nontoxic Halide
 Perovskite Materials for High-Efficiency Solar Cells. Adv. Funct. Mater., 2019, 29
 (23). https://doi.org/10.1002/adfm.201804354.
- Islam, M. S.; Wang, S.; Hall, A. T.; Mo, Y. First-Principles Computational Design
 and Discovery of Solid-Oxide Proton Conductors. *Chem. Mater.*, 2022, 34 (13),
 5938–5948. https://doi.org/10.1021/acs.chemmater.2c00867.
 - (30) Kresse, G.; Furthmüller, J. Efficient Iterative Schemes for *Ab Initio* Total-Energy Calculations Using a Plane-Wave Basis Set. *Phys. Rev. B*, **1996**, *54* (16), 11169–11186. https://doi.org/10.1103/PhysRevB.54.11169.
 - (31) Perdew, J. P.; Yue, W. Accurate and Simple Density Functional for the Electronic Exchange Energy: Generalized Gradient Approximation. *Phys. Rev. B*, **1986**, *33* (12), 8800–8802. https://doi.org/10.1103/PhysRevB.33.8800.
 - (32) Perdew, J. P.; Wang, Y. Accurate and Simple Analytic Representation of the Electron-Gas Correlation Energy. *Phys. Rev. B*, **1992**, *45* (23), 079904. https://doi.org/10.1103/PhysRevB.45.13244.
- Kresse, G.; Joubert, D. From Ultrasoft Pseudopotentials to the Projector
 Augmented-Wave Method. *Phys. Rev. B*, 1999, *59* (3), 1758–1775.
 https://doi.org/10.1103/PhysRevB.59.1758.

636

637

638

639

640

641

642

- 647 (34) Blöchl, P. E. Projector Augmented-Wave Method. *Phys. Rev. B*, **1994**, *50* (24), 17953–17979. https://doi.org/10.1103/PhysRevB.50.17953.
- (35) Ong, S. P.; Richards, W. D.; Jain, A.; Hautier, G.; Kocher, M.; Cholia, S.; Gunter, D.; Chevrier, V. L.; Persson, K. A.; Ceder, G. Python Materials Genomics
 (Pymatgen): A Robust, Open-Source Python Library for Materials Analysis. *Comput. Mater. Sci.*, 2013, 68, 314–319.
 https://doi.org/10.1016/j.commatsci.2012.10.028.
- (36) Jain, A.; Ong, S. P.; Hautier, G.; Chen, W.; Richards, W. D.; Dacek, S.; Cholia, S.;
 Gunter, D.; Skinner, D.; Ceder, G.; Persson, K. A. Commentary: The Materials

- Project: A Materials Genome Approach to Accelerating Materials Innovation. *APL Mater.*, **2013**, *1* (1), 011002. https://doi.org/10.1063/1.4812323.
- (37) Dudarev, S. L.; Botton, G. A.; Savrasov, S. Y.; Humphreys, C. J.; Sutton, A. P.
 Electron-Energy-Loss Spectra and the Structural Stability of Nickel Oxide: An
 LSDAU Study. *Phys. Rev. B*, 1998, 57 (3).
 https://doi.org/10.1103/PhysRevB.57.1505.
- (38) Wang, L.; Maxisch, T.; Ceder, G. Oxidation Energies of Transition Metal Oxides
 within the GGA+U Framework. *Phys. Rev. B*, 2006, 73 (19).
 https://doi.org/10.1103/PhysRevB.73.195107.
- 665 (39) Monkhorst, H. J.; Pack, J. D. Special Points for Brillonin-Zone Integrations. *Phys. Rev. B*, **1976**, *13* (12). https://doi.org/10.1103/PhysRevB.13.5188.

668

- (40) Wu, Y.; Lazic, P.; Hautier, G.; Persson, K.; Ceder, G. First Principles High Throughput Screening of Oxynitrides for Water-Splitting Photocatalysts. *Energy Environ. Sci.* **2013**, *6* (1), 157–168. https://doi.org/10.1039/c2ee23482c.
- 670 (41) Saal, J. E.; Kirklin, S.; Aykol, M.; Meredig, B.; Wolverton, C. Materials Design 671 and Discovery with High-Throughput Density Functional Theory: The Open 672 Quantum Materials Database (OQMD). *JOM.* **2013**, *65* (11), 1501–1509. 673 https://doi.org/10.1007/s11837-013-0755-4.
- 674 (42) Ong, S. P.; Wang, L.; Kang, B.; Ceder, G. Li Fe P O₂ Phase Diagram from
 675 First Principles Calculations. *Chem. Mater.*, **2008**, *20* (5), 1798–1807.
 676 https://doi.org/10.1021/cm702327g.
- Jain, A.; Hautier, G.; Ong, S. P.; Moore, C. J.; Fischer, C. C.; Persson, K. A.;
 Ceder, G. Formation Enthalpies by Mixing GGA and GGA + U Calculations. *Phys. Rev. B*, 2011, 84 (4). https://doi.org/10.1103/PhysRevB.84.045115.
- 680 (44) Suthirakun, S.; Ammal, S. C.; Muñoz-García, A. B.; Xiao, G.; Chen, F.; zur Loye, H. C.; Carter, E. A.; Heyden, A. Theoretical Investigation of H₂ Oxidation on the Sr ₂Fe_{1.5}Mo_{0.5}O₆ (001) Perovskite Surface under Anodic Solid Oxide Fuel Cell Conditions. *J. Am. Chem. Soc.*, **2014**, *136* (23), 8374–8386. https://doi.org/10.1021/ja502629j.
- 685 (45) Bucher, E.; Sitte, W.; Klauser, F.; Bertel, E. Oxygen Exchange Kinetics of La_{0.58}Sr_{0.4}Co _{0.2}Fe_{0.8}O₃ at 600 °C in Dry and Humid Atmospheres. *Solid State Ion.*, **2011**, *191* (1), 61–67. https://doi.org/10.1016/j.ssi.2011.03.019.
- (46) Dunstan, M. T.; Jain, A.; Liu, W.; Ong, S. P.; Liu, T.; Lee, J.; Persson, K. A.; Scott,
 S. A.; Dennis, J. S.; Grey, C. P. Large Scale Computational Screening and
 Experimental Discovery of Novel Materials for High Temperature CO₂ Capture.
 Energy Environ. Sci., 2016, 9 (4), 1346–1360. https://doi.org/10.1039/c5ee03253a.

- (47) Kröger, F. A.; Vink, H. J. Relations between the Concentrations of Imperfections in
 Solids. J. Phys. Chem. Solids, 1958, 5 (3), 208–223. https://doi.org/10.1016/0022-3697(58)90069-6.
- (48) Freysoldt, C.; Grabowski, B.; Hickel, T.; Neugebauer, J.; Kresse, G.; Janotti, A.;
 van de Walle, C. G. First-Principles Calculations for Point Defects in Solids. *Rev.* Mod. Phys., 2014, 86 (1), 253–305. https://doi.org/10.1103/RevModPhys.86.253.
- Lindman, A.; Helgee, E. E.; Wahnström, G. Comparison of Space-Charge
 Formation at Grain Boundaries in Proton-Conducting BaZrO₃ and BaCeO₃. *Chem. Mater.*, 2017, 29 (18), 7931–7941. https://doi.org/10.1021/acs.chemmater.7b02829.
- (50) Sun, W.; Dacek, S. T.; Ong, S. P.; Hautier, G.; Jain, A.; Richards, W. D.; Gamst, A.
 C.; Persson, K. A.; Ceder, G. The Thermodynamic Scale of Inorganic Crystalline
 Metastability. *Science*, 2016, 2 (11), 1600225.
 https://doi.org/10.1126/sciadv.1600225.
 - (51) Zhang, W.; Hu, Y. H. Progress in Proton-Conducting Oxides as Electrolytes for Low-Temperature Solid Oxide Fuel Cells: From Materials to Devices. *Energy Sci. Eng.* **2021**, *9*, 984–1011. https://doi.org/10.1002/ese3.886.

706

707

708

709

- (52) Ryu, K. H.; Haile, S. M. Chemical Stability and Proton Conductivity of Doped BaCeO₃–BaZrO₃ Solid Solutions. *Solid State Ion.* **1999**, *125* (1–4), 355–367. https://doi.org/10.1016/S0167-2738(99)00196-4.
- (53) Fabbri, E.; D'Epifanio, A.; Di Bartolomeo, E.; Licoccia, S.; Traversa, E. Tailoring the Chemical Stability of Ba(Ce0.8-xZr_x)Y_{0.2}O_{3-δ} Protonic Conductors for Intermediate Temperature Solid Oxide Fuel Cells (IT-SOFCs). *Solid State Ion*.
 2008, 179 (15–16), 558–564. https://doi.org/10.1016/j.ssi.2008.04.002.
- 715 (54) Yamazaki, Y.; Blanc, F.; Okuyama, Y.; Buannic, L.; Lucio-Vega, J. C.; Grey, C. P.; Haile, S. M. Proton Trapping in Yttrium-Doped Barium Zirconate. *Nat. Mater.*, **2013**, *12* (7), 647–651. https://doi.org/10.1038/nmat3638.
- 718 (55) Kang, S. G.; Sholl, D. S. First-Principles Investigation of Chemical Stability and 719 Proton Conductivity of M-Doped BaZrO₃ (M=K, Rb, and Cs). *J. Am. Ceram. Soc.* 720 **2017**, 100 (7), 2997–3003. https://doi.org/10.1111/jace.14839.
- (56) Sun, W.; Liu, M.; Liu, W. Chemically Stable Yttrium and Tin Co-Doped Barium
 Zirconate Electrolyte for next Generation High Performance Proton-Conducting
 Solid Oxide Fuel Cells. Adv. Energy Mater. 2013, 3 (8), 1041–1050.
 https://doi.org/10.1002/aenm.201201062.
- Dawson, J. A.; Miller, J. A.; Tanaka, I. First-Principles Insight into the Hydration
 Ability and Proton Conduction of the Solid State Proton Conductor, y and Sn Co Doped BaZrO₃. Chem. Mater.. 2015, 27 (3), 901–908.
 https://doi.org/10.1021/cm504110y.

Jeong, Y. C.; Kim, D. H.; Kim, B. K.; Kim, Y. C. Migration and Interaction of 729 Multi-Protons in Zinc-Doped Barium Zirconate. Kor. J. Met. Mater. 2011, 49 (12), 730 731 977–982. https://doi.org/10.3365/KJMM.2011.49.12.977. 732 (59) Han, D.; Uda, T. The Best Composition of an Y-Doped BaZrO₃ Electrolyte: 733 Selection Criteria from Transport Properties, Microstructure, and Phase Behavior. J. Mater. Chem A. 2018, 6 (38), 18571–18582. https://doi.org/10.1039/c8ta06280c. 734 Ueno, K.; Hatada, N.; Han, D.; Uda, T. Thermodynamic Maximum of Y Doping 735 736 Level in Barium Zirconate in Co-Sintering with NiO. J. Mater. Chem. A. 2019, 7 737 (12), 7232–7241. https://doi.org/10.1039/c8ta12245h. 738

For Table of Contents Only

